Technical report

A CT-, PET- and MR-imaging-compatible hyperbaric pressure chamber for baromedical research

Kasper Hansen, Esben SS Hansen, Lars P Tolbod, Martin C Kristensen, Steffen Ringgaard, Alf O Brubakk and Michael Pedersen

Abstract

(Hansen K, Hansen ESS, Tolbod LP, Kristensen MC, Ringgaard S, Brubakk AO, Pedersen M. A CT-, PET- and MR-imaging-compatible hyperbaric pressure chamber for baromedical research. *Diving and Hyperbaric Medicine*. 2015 December;45(4):247-254.)

Objectives: We describe the development of a novel preclinical rodent-sized pressure chamber system compatible with computed tomography (CT), positron emission tomography (PET) and magnetic resonance imaging (MRI) that allows continuous uncompromised and minimally invasive data acquisition throughout hyperbaric exposures. The effect of various pressures on the acquired image intensity obtained with different CT, PET and MRI phantoms are characterised.

Material and methods: Tissue-representative phantom models were examined with CT, PET or MRI at normobaric pressure and hyperbaric pressures up to 1.013 mPa. The relationships between the acquired image signals and pressure were evaluated by linear regression analysis for each phantom.

Results: CT and PET showed no effect of pressure per se, except for CT of air, demonstrating an increase in Hounsfield units in proportion to the pressure. For MRI, pressurisation induced no effect on the longitudinal relaxation rate (R_1), whereas the transverse relaxation rate (R_2) changed slightly. The R_2 data further revealed an association between pressure and the concentration of the paramagnetic nuclei gadolinium, the contrast agent used to mimic different tissues in the MRI phantoms.

Conclusion: This study demonstrates a pressure chamber system compatible with CT, PET and MRI. We found that no correction in image intensity was required with pressurisation up to 1.013 mPa for any imaging modality. CT, PET or MRI can be used to obtain anatomical and physiological information from pressurised model animals in this chamber.

Key words

Pressure chambers; radiological imaging; pressure; animal model; equipment; hyperbaric research

Introduction

Computed tomography (CT), positron emission tomography (PET) and magnetic resonance imaging (MRI) are routinely used to visualise internal morphology and quantify basic physiological parameters non-invasively. While CT visualises particularly hard tissues, MRI can visualise soft tissue anatomy and is capable of measuring certain physiological parameters and metabolites. PET uses synthesized, radiolabelled tracers, which mimic endogenous bioactive species, to examine specific metabolic processes. Combination of such imaging systems and pressure chambers has the potential to non-invasively investigate fundamental structural, physiological and metabolic processes in the acute phases of compression and decompression: stages in experimental barometric research studies which have traditionally been very challenging due to the limited accessibility to the model animal inside the pressure chamber.

Specialised chambers have been constructed for preclinical and animal research,[1,2] but these systems unfortunately are incompatible with most medical imaging systems. Recently a commercial manufacturer has introduced a preclinical MRI-compatible pressure chamber, available up to a relatively low pressure.[3] We describe a simple, cost-effective, imaging-compatible pressure chamber system that facilitates simultaneous CT, PET and/or MRI of rodents over a range of pressures from 101.3 kPa to 1.013 mPa (equivalent to 90 metres' seawater (msw)).

Materials and methods

CONSIDERATIONS

Materials used for pressure chamber systems should comply with basic CT, PET and MRI physics requirements. In short, because CT uses characteristic X-ray attenuation to create shadow images of the traversing radiation (photons), the materials used should neither block nor scatter the X-ray radiation. Similarly for PET, the characteristic 511 keV photons emitted from the site of positron annihilation should traverse the chamber material readily. On the other hand, MRI systems use extremely strong magnetic fields together with powerful radiofrequency pulses to produce an image that is dependent on the distribution of hydrogen in the body, so the material must be completely non-magnetic, non-electrically conductive, and not disturb the emitted radio frequencies.

Figure 1

System overview; 1 – imaging system (CT, PET or MRI); 2 – imaging compatible pressure chamber; 3 and 4 – pressure and temperature sensors (optical technology); 5 – optical fibre extension cables (10 m long); 6 – flexible high-pressure polyamide pneumatic tubing (Ø/ø: 4/6 mm, 10 m long) connected to pressure chamber and pressure control unit through acetal-based snap-in pneumatic plugs; 7 – Pressure-tight cable and catheter penetrations; 8 – optical to digital signal converter; 9 – A/D converter; 10 – sensor output interface; 11 – interface for solenoid valve control; 12 – proportional solenoid valve for gas-inlet; 13 – plunger valve for gas-output control; 14 – pressure reducing valve (displaying safety redundancy; hence, the inlet pressure is reduced well below the pressure limits of the system components); 15 – compressed gas cylinder (allows the use of any premixed gas mixture); 16 – computer system (for pressure profile execution and data acquisition through various third-party software providers). Full details of the specific equipment used is available from the authors.

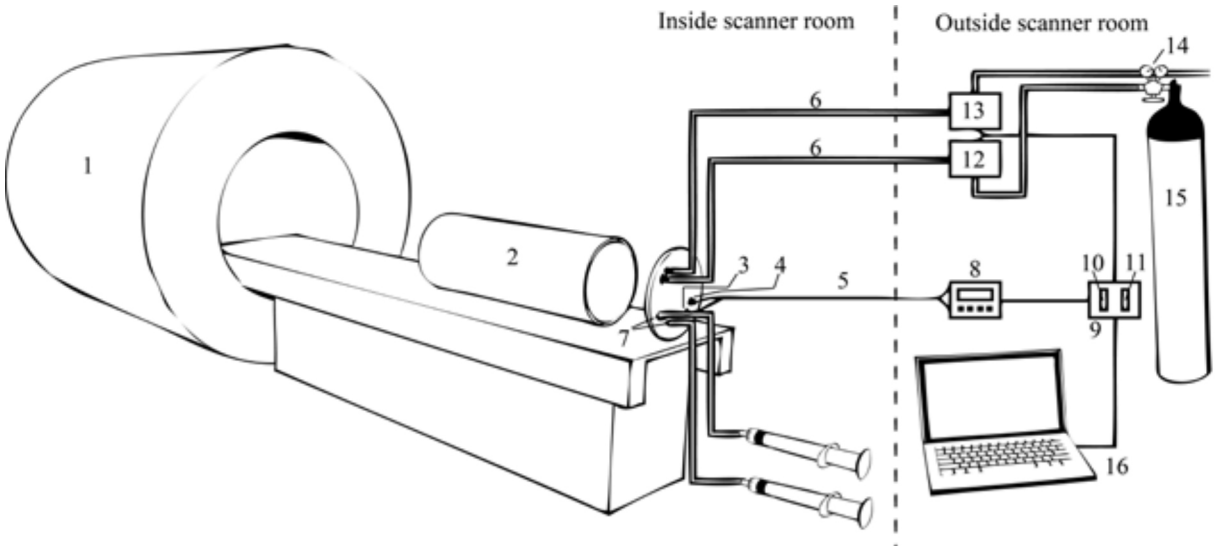

DESIGN

Figure 1 shows a schematic drawing of the pressure chamber system. The non-magnetic pressure chamber is positioned inside the scanner and connected to an automated pressure control device that, for use in MRI, must be located outside the scanner room. PVC rods, PVC union flanges and acetal-based snap-in pneumatic plugs used for the system were purchased CE-certified for working pressures up to 1.621 mPa. A PVC-union flange was mounted to each end of the 400 mm long PVC-rod (internal/external diameter: 100/110 mm) using PVC glue. Transparent polycarbonate plate (thickness 15 mm) was cut to precisely fit the recess inside a threaded union-flange-cap, thereby aiding as end plates compressing the axially positioned O-ring seals in the union-flanges. Before use, the system was safety tested through multiple pressurisations to double the intended working pressure (to 2.026 MPa). Additional component details are included in the Figure 1 legend.

PRESSURISATION AND INSTRUMENTATION

Compressed atmospheric gas (air) was delivered through flexible polyamide hoses, connected to the control unit and pressure chamber through snap-in pneumatic plugs. Two hoses were fitted to the pressure chamber, one in either end to ensure efficient gas exchange and to avoid excessive carbon dioxide (CO_2) build up during an animal experiment. Accordingly, chalk scrubbers inside the pressure chamber could be used to remove CO_2 further in animal experiments. Pressure-tight penetrations allowed insertion of fibr optic pressure and temperature probes. Further, PE-hoses were used to construct a circulating water-loop, allowing temperature feedback regulation (this option was not used during phantom scans). The pressure and temperature inside the chamber may be controlled remotely from the scanner's control room. An automated pressure-control unit was built to ensure reproducible pressure profiles while scanning, using LabVIEW 2013 software (National Instruments).

SCANNING PROCEDURES AND PHANTOMS

The effect of hyperbaric conditions on the acquired CT, PET and MRI images were investigated using phantom models. Individual phantoms were scanned multiple times including initial scans at normobaric pressure (101.3 kPa) outside the pressure chamber, followed by normobaric scans inside the pressure chamber. Additional scans were performed at pressures of 203, 405, 608, 810 kPa, 1.013 mPa, and a final scan after a short decompression period.

CT

The phantoms were homogeneous cylindrical material rods (length 5 cm, diameter 2 cm) of acrylic, polypropylene, polyethylene, teflon or bone, immersed in sterile water. Two vials containing demineralised water and air inside the pressure chamber were also used as phantoms.

PET

Two vials (PET phantom A, PET phantom B) containing 35 mL demineralised water with initial radioactive gamma-activities of 40 and 80 kBq·mL^{-1} respectively provided by addition of the PET tracer ^{18}Fluorodeoxyglucose.

MRI

A gadolinium (Gd)-containing contrast agent (279.3 mg Gd·mL^{-1}, Dotarem) was dissolved in demineralised water in concentrations of 0, 0.5, 1.0 and 2.0 mM, and the solutions were degassed by heating to 80°C in an ultrasound device for 120 min. This process provoked nucleation of dissolved gas, which could be removed by applying vacuum using gastight syringes pulled hard to provoke further nucleation after cooling to room temperature. Any visible gas inside the syringes was carefully removed. MRI phantoms were kept in filled, airtight vials to avoid gas exchange with the surroundings. The MRI phantoms were kept at room temperature (21°C) during the study period.

IMAGING SYSTEMS AND ACQUISITION PROTOCOL

CT

GE Medical Systems (Discovery 690®). Rotation time: 0.5 s, energy level 120 kV, tube current: 200 mA, slice thickness: 1.25 mm, slice spacing: 0.63 mm, feed/rotation: 39.38 mm.

PET

GE Medical Systems (Discovery 690®). Scanning time: 3 min, number of slices: 47, image matrix size: 1.82 × 1.82 × 3.27 mm^3. Images were reconstructed using the VuePoint HD SharpIR algorithm (3 iterations, 24 subsets, 4 mm 2D Gaussian post filter in the transaxial plane and a 3-point convolution axial filter ('light' filter [1, 6, 1]/8)) with standard CT attenuation and scatter correction.

MRI:

T Siemens MRI system (Magnetom Skyra®). The pressure chamber fitted exactly into a 32-channel transmit/receive knee radiofrequency coil. For R_1 measurements, a Look-Locker approach (inversion-recovery True-FISP sequence) with 288 inversion-times was used, whereas a spin-echo sequence with 16 echo times (TE) (40–640 ms) was used for R_2 measurements. R_1 protocol: scanning time: 3:23 min, resolution matrix: 80 × 44, FOV: 153 × 84 mm^2, slice thickness: 7 mm, repetition time: 3.12 ms, TE: 1.35 msec, flip angle: 5°. R_2 protocol: scanning time: 2:50 min, resolution matrix: 64 × 41, FOV: 75 × 75 mm^2, slice thickness: 7.0 mm, repetition time: 4000 ms, TE: 40–640 ms.

Figure 2

Representative results from CT scans of phantoms, teflon (A), and air (B), respectively; scans were performed at normobaric pressure both outside and inside the pressure chamber 101.3 kPa and at various pressures between 203 kPa and 1.013 MPa; values are the relative % differences from normobaric values inside the pressure chamber (mean ± SD), *n*-values as in Table 1. The slope of the regression for Teflon phantom was not significantly different from zero, whereas the slope of the air regression (B) was (N.B. these slopes are calculated from the percentage change of HU with pressure, whereas slopes reported in Table 1 are calculated directly from HU- values).

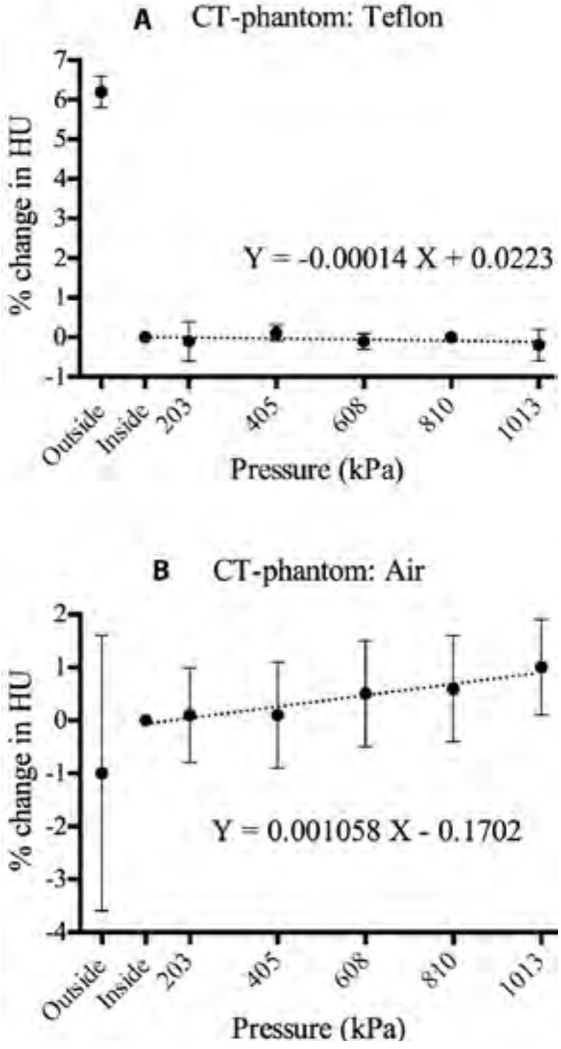

DATA ANALYSIS AND STATISTICS

Image analyses were performed with the OsiriX software (version 5.5.1, 64-bit). Statistical analyses were performed in STATA 12.0 and PRISM 6. Linear regression analysis was used to test the null hypothesis that pressure per se had no significant effect on the image signal. CT and MRI analyses were performed on raw data, while PET data were normalised before analysis because the data were obtained over three individual acquisitions, which resulted in slightly

Figure 3

PET scans of two ^{18}Fluorodeoxyglucose-based solutions with initial activities of 40 (A) and 80 kBq·mL^{-1} and (B), respectively; scans were performed at normobaric pressure both outside and inside the chamber. Values are relative % differences from normobaric values inside the chamber (mean ± SD); *n*-values as reported in Table 2; the slopes of the regressions were not significantly different from zero.

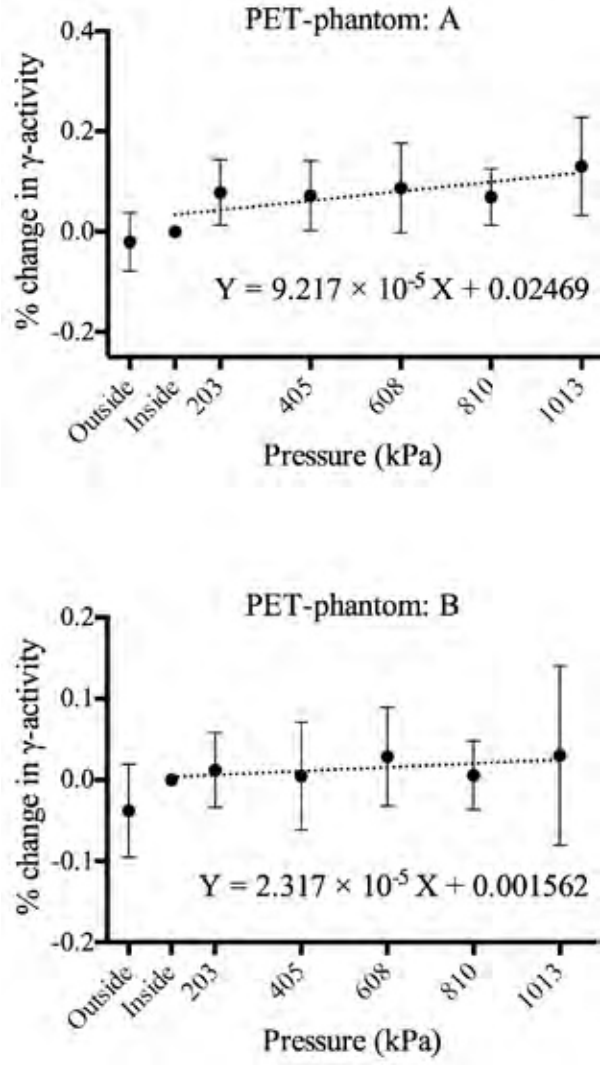

different individual phantom-activities. The PET signal was corrected for radioactive decay.

A linear regression analysis was used to test whether the slope (the derivative of image intensity versus pressure) was significantly different from zero. Equation [1] describes the linear relationship for CT, Eq. [2] is for PET, and Eq. [3] is for MRI, assuming that different Gd-concentrations represent various magnetic relaxation properties of tissues:

$$HU_{(P)} = HU_{0(P=101\ kPa,\ Phantommaterial)} + \kappa' \times P \quad [1]$$

$$Activity_{(P)} = A_{0(P=101kPa)} + \kappa' \times P'' \quad [2]$$

$$R_{1,2(P,[Gd])} = R_{1,2(P=101kPa,[Gd]=0)} + r_{1,2(P)} \times P + r_{1,2([Gd])} \times [Gd] \quad [3]$$

Figure 4

MRI scans using (A) T_1- and (B) T_2-weighted sequences of four degassed Gd-based phantoms ($R_1 = T_1^{-1}$, $R_2 = T_2^{-1}$); scans were performed at normobaria both outside and inside the chamber. Values are relative % differences from normobaric values obtained of phantoms inside the chamber (mean ± SD); all four phantoms were scanned at equal pressure(s) (white and grey areas indicate constant pressure equivalent to tick markings below) but data points have been nudged to avoid superimposed points; refer to Table 3 for regression coefficients and *n*-values.

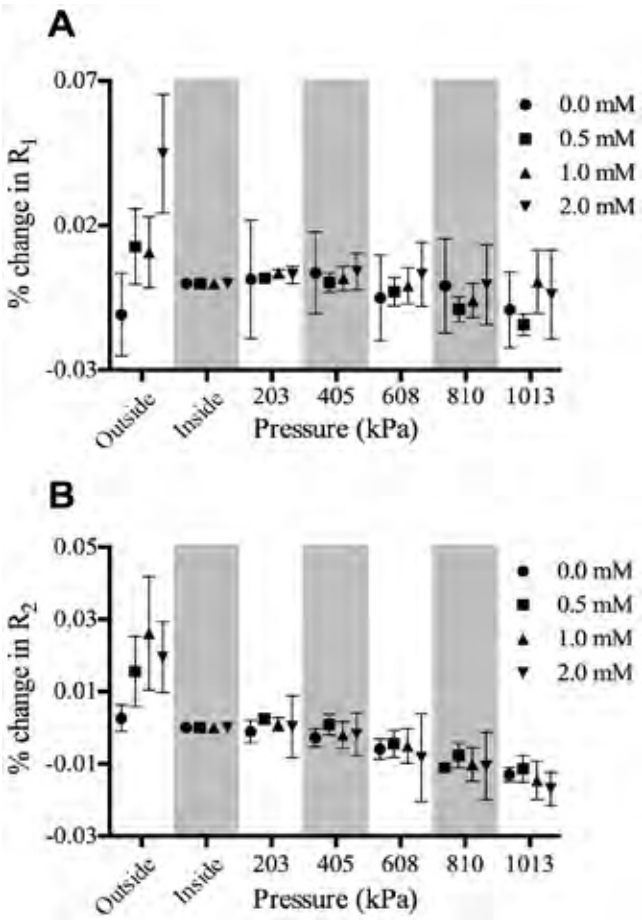

where P is total pressure in units of kPa, and κ' and κ'' are specific material constants reflecting the material density to electromagnetic radiation for CT and PET, respectively. R_1 and R_2 are the longitudinal and transversal proton relaxation rates, $r_{1(P)}$ and $r_{2(P)}$ are longitudinal and transversal pressure-specific relaxivity constants, and $r_{1([Gd])}$ and $r_{2([Gd])}$ are the longitudinal and transversal Gd (paramagnetic)-specific relaxivity constants (where relaxivity denotes a change in relaxation per change in pressure or [Gd], respectively).

Results

We observed that pressure changes had no visible effects (e.g., noise or artefacts) on any phantom. The CT-measured HU for the teflon phantom was slightly reduced inside the pressure chamber compared to outside the chamber at normobaric conditions (Figure 2A). This is consistent with

Table 1
Linear regression analysis of CT phantoms scanned during pressurisation (101.3–1,013 kPa); intercept values are material-specific Hounsfield Units; the number of CT scans at each individual pressure were (kPa/*n*-value): 101(outside)/8, 101(inside)/4, 203/3, 405/3, 608/3, 811/3, and 1013/2.

CT phantoms	Regression (slope ± SEM)	Test values (slope)	Intercept (HU units ± SEM)	Test values (intercept)	R^2
Teflon	-0.0013 ± 0.0035	t = -0.38, P = 0.71	1390.07 ± 2.10	t = 661.53, P < 0.01	0.008
Bone	-0.0007 ± 0.0024	t = -0.30, P = 0.77	940.63 ± 1.43	t = 656.37, P < 0.01	0.005
Polypropylene	-0.0010 ± 0.0017	t = -0.59, P = 0.57	-98.10 ± 0.99	t = -98.68, P < 0.01	0.02
Acrylic	0.0005 ± 0.0021	t = 0.22, P = 0.83	123.39 ± 1.24	t = 99.90, P < 0.01	0.003
Polyethylene	0.0001 ± 0.0012	t = 0.08, P = 0.94	-85.33 ± 0.71	t = -119.77, P < 0.01	0.0004
Water	0.0008 ± 0.0013	t = 0.59, P = 0.56	-1.32 ± 0.79	t = -1.66, P = 0.107	0.012
Air	0.0107 ± 0.0008	t = 13.64, P < 0.01	-977.48 ± 0.46	t = -2126.35, P < 0.01	0.89

CT beam hardening caused by the PVC material used to construct the pressure chamber. The beam hardening artefact was, however, too small to have any measurable effect on the attenuation- and scatter-corrected PET images (Figures 3A and 3B). No magnetic inhomogeneity or RF disturbances were observed in the MRI data (Figures 4A and 4B).

The squared linear regression coefficient (R^2) varied greatly (range 0.001–0.99, Tables 1 and 2). We found very little effect of pressure on the signal obtained using the three imaging modalities. Representative graphs showing the acquired signal relative to the signal obtained inside the pressure chamber at normobaric pressure; CT (Figure 2A and 2B), PET (Figures 3A and 3B) and MRI (Figures 4A and 4B). The slopes of the linear regressions for the CT and PET data were not significantly different from zero, with the exception of the slope of CT scans of air, demonstrating a slope of 0.0107 ± 0.0008 HU × kPa^{-1}; significantly different from zero (t = -13.64, P < 0.01; Table 1). The slopes for CT phantoms in Table 1 were calculated directly from HU values, whereas the slopes in Figure 2 were calculated from the percentage change of HU with pressure and accordingly differ slightly from the values in Table 1. Linear regression analysis of PET phantoms scanned during pressurisation were not significantly different from zero.

For MRI, the longitudinal relaxivity (r_1) of Gd-phantoms of 0.0, 1.0, and 2.0 mM were not significantly affected by pressure, whereas the 0.5 mM phantom, in contrast, was significantly affected by -0.000037 ± 0.000015 s^{-1} × kPa^{-1} (mean ± SEM) (t = -2.98, P = 0.005; Table 3). The transversal relaxivity (r_2) of the Gd-phantoms were all slightly, but not significantly, affected by pressure (maximal effect was found for the 2.0 mM; -0.00019 ± 0.00006 s^{-1} × kPa^{-1} (mean ± SEM), t = -3.13, P = 0.004; Table 3). The MRI relaxivities were plotted against [Gd] (Figure 5), and

Table 2
Linear regression analysis of PET phantoms scanned during pressurisation were not significantly different from zero; scans at individual pressures were (kPa/*n*-value): 101(outside)/8, 101(inside)/4, 203/3, 405/3, 608/3, 811/3, and 1013/2.

PET phantom	Regression slope (± SEM)	Test values (slope)	R^2
A	0.00005 ± 0.00003	t = 1.47, P = 0.16	0.12
B	0.00003 ± 0.00002	t = 1.25, P = 0.23	0.09

Table 3
MRI of Gd-phantoms scanned during pressurisation (101–1,013 kPa); the pressure specific relaxivities (r_1 and r_2, s^{-1} × kPa^{-1}, respectively) were established through linear regression analysis of pressurised degased phantoms, i.e., the $r_{1,2}$ corresponds to changes in $R_{1,2}$ per change in kPa. The number of MRI-scans for all phantoms (in both r_1 and r_2) at each individual pressure were (kPa/*n*-value): 101(outside)/6, 101(inside)/6, 203/6, 405/6, 608/6, 811/6 and 1013/6.

MRI phantoms [Gd]		Relaxivity (±SEM)	Test values	R^2
r_1	0 mMol	-0.0000049 ± 0.0000024	t = -2.01, P = 0.052	0.11
	0.5 mM	-0.000037 ± 0.000015	t = -2.98, P = 0.005*	0.21
	1.0 mM	-0.0000192 ± 0.00002	t = -0.96, P = 0.343	0.03
	2.0 mM	-0.0000413 ± 0.000055	t = -0.75, P = 0.457	0.02
r_2	0 mM	-0.0000072 ± 0.0000011	t = -6.68, P < 0.001*	0.57
	0.5 mM	-0.00004 ± 0.0000098	t = -4.08, P < 0.001*	0.33
	1.0 mM	-0.000085 ± 0.000029	t = -2.98, P = 0.005*	0.21
	2.0 mM	-0.00019 ± 0.00006	t = -3.13, P = 0.004*	0.22

Figure 5
A possible interaction between pressure (kPa) and [Gd] was evaluated by plotting longitudinal (A) and transversal (B) pressure specific relaxivities (i.e., r_1 and r_2 values from Table 3) against [Gd]; the slope of r_2 was significantly different from zero, whereas the slope of r_1 was not.

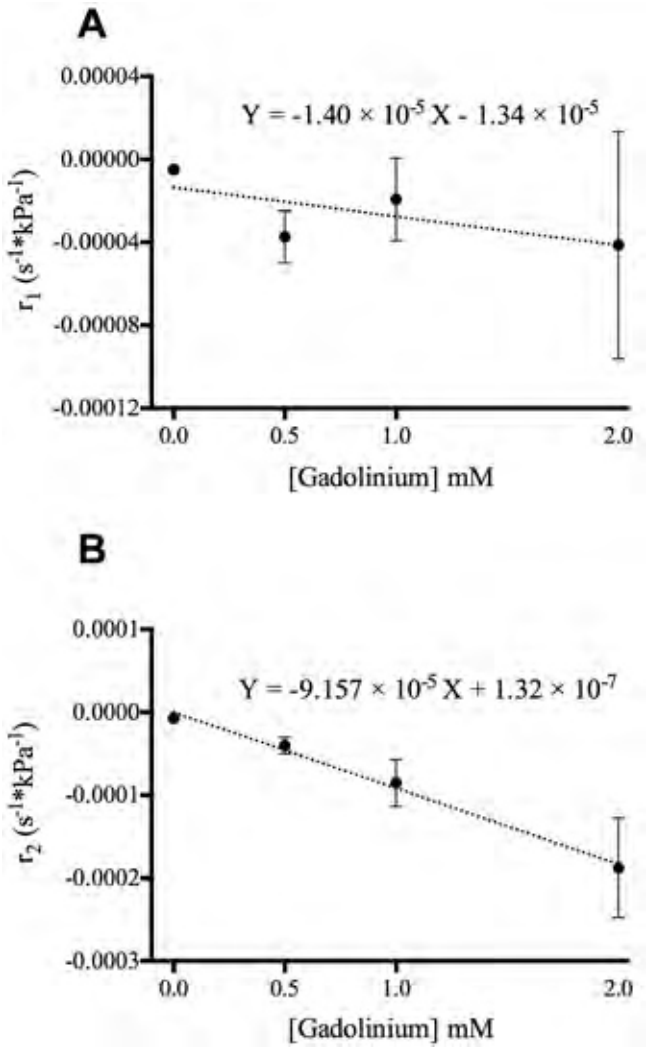

linear regressions were performed to test for interactions between pressure per se and the concentration of gadolinium. There was no significant interaction between pressure and [Gd] for longitudinal relaxivity ($-1.40\times10^{-5} \pm 9.86\times10^{-6}$ $s^{-1} \times kPa^{-1} \times [Gd]^{-1}$ (mean ± SD), F = 2.01, P = 0.29, R^2 = 0.50), whereas a significant interaction on the transversal relaxivity resulted in a regression slope of $-9.157\times10^{-5} \pm 5.772\times10^{-6}$ $s^{-1} \times kPa^{-1} \times [Gd]^{-1}$ (mean ± SD), F = 251.7, P = 0.0039, R^2 = 0.99 (Figure 5).

Discussion

The aim of this study was to develop a CT-, PET- and MRI-compatible hyperbaric pressure chamber system and to quantify the effect of pressure per se over a range of pressures up to 1.013 MPa on the acquired signals in appropriate tissue-representative phantoms. We found that changes in pressure had no important influence on the image signals.

Recent studies using imaging-based systems in the investigation of diving-related symptoms of decompression sickness (DCS), have mainly included scans performed after pressure exposures, either acutely[4,5] or days, month or years after pressure exposure(s).[6–10] CT, PET and MRI could be used during the hyperbaric or hypobaric period if the pressure chamber materials comply strictly with the underlying physics of the scanner systems. Today, imaging compatible pressure chamber systems have only been used in a few studies; two studies of hyperbaric oxygen (maximum pressurisation to 405 kPa) and one for CT examination of lung compression in seal and dolphin cadavers (using a water-filled system pressurised up to 1.220 mPa).[11–13]

With CT, there is a beam-hardening effect resulting from absorption of low-energy X-rays in the pressure chamber material, with the effect that only the higher energies of the X-ray spectrum are traversing the pressure chamber and internal objects. Accordingly, these X-rays also penetrate the scanned object more easily, resulting in a small but evident HU-shift as demonstrated in Figure 2.[14,15] However, any contributing effects on the image signal induced by the pressure chamber itself are only problematic when comparing the signal acquired from objects outside the chamber with the acquired signal of the phantom inside the chamber. All data obtained from the CT phantoms (Table 1) were statistically unaffected by elevated pressure with the exception of air. The increase in X-ray density in the pressurised air corresponded to the linear increase in air density with pressure (Table 1).

Changes in pressure did not significantly affect the PET signal obtained from the two solutions of ^{18}Fluorodeoxyglucose (Table 2 and Figure 3) and no important artefacts were induced by the pressure chamber system.

For MRI, the use of degassed distilled water phantoms at 21°C revealed a non-significant effect of pressure with a slightly negative longitudinal relaxivity (Table 3, Figure 4A). Note, however, that the relaxation properties of water molecules depend on the applied magnetic field. In this study, we used a magnetic field strength of 3 Tesla, and the resulting T_1-relaxation ($1/T_1 = R_1$) of degassed phantoms at normobaric pressure was 1988 ± 7.3 ms (mean ± SEM; data not shown). Using a temperature correction of distilled water at 3 T of 0.106 s × °C^{-1} (SEM: 0.009 s × °C^{-1})[16], our measured relaxation rate of 0.27 s^{-1} (calculated from the formula: 1.988 s + 16°C × 0.106 s × °C^{-1}) is comparable to values obtained in degassed distilled water phantoms at 37°C of 0.21 s^{-1} and 0.22 s^{-1} respectively on a 1.5 T system.[17,18] In the four Gd-containing solutions used, only the 0.5 mM phantom resulted in a regression slope significantly different from zero. The transversal relaxivity (r_2) was significantly reduced by pressure for all four Gd-phantoms, apparently

with an impact increasing proportionally with pressure (Table 3, Figure 4B). This finding is apparent from a graphical plot that shows the pressure-specific transversal relaxivity (r_2, $s^{-1} \times kPa^{-1}$) as a function of Gd-concentration (Figure 5B), demonstrating a negative regression significantly different from zero (Figures 4B and 5B).

Gaseous oxygen, unlike most other gases, is paramagnetic due to its two unpaired electrons and, thus, it has the potential to affect the magnetic properties of water in an MRI system in terms of R_1 and R_2.[19] The intermediate dipole-dipole interactions of oxygen molecules with protons should add a linearly dependent contribution to the relaxation rate in accordance with Solomon-Bloembergen equations.[20] Therefore, the method of degassing the Gd-phantoms in this study should be addressed. According to one study, 10–20% of the liquid is needed to evaporate during boiling under high vacuum to degas a solvent completely.[21] As described earlier, another method was employed in this study for practical reasons. Therefore, there could have been air (including oxygen) dissolved in the Gd-phantoms, having a potential contribution to both R_1 and R_2. Accordingly, minor differences in oxygenation between the phantoms could explain why the relaxivity of the 0.5 mM phantom was significantly modified by pressure, while the 0, 1.0 and 2.0 mM Gd-phantoms were not. Besides, because the T_2-weighted sequences are inherently susceptible to fluctuations in the magnetic field, diamagnetic gaseous oxygen leftovers from an incomplete degassing could explain why the transversal relaxivity is significantly affected by pressurisation for all phantoms.

The results from the phantom scans suggest that Eq. [1] and [2] may be discarded with the exception of CT imaging of compressible gases. In MRI, we found that an additional second-order term may be included for the R_2 relaxation rate, and Eq. [3] for R_2 should be modified as follows:

$$R_{2(P,[Gd])} = R_{2(P = 101\,kPa,\ [Gd] = 0)} + r_{2(P)} \times P + r_{2([Gd])} \times [Gd] + r_2' \times [Gd] \times P \quad [4]$$

Where r_2' is the first-order relaxivity constant for the combined pressure and gadolinium-concentration term. However, because the contribution of the pressure-modified transversal relaxivity to the resulting transversal relaxation is extremely small relative to the contribution from the imaged tissue (or phantom Gd-concentration), for pressures relevant to baro-physiologic and medical research, we believe that contributions from higher-order terms are small, and Eq. [3] would be a precise approximation to the transversal relaxation rate.

We found that no correction in image intensity was required for CT, PET or MRI up to a pressure of 1.013 mPa; that is, there were negligible effects of pressure per se on the signals obtained. However, for MRI, the signal modification associated with increasing oxygen tension of blood and tissues with pressure must be considered carefully. These findings represent a fundamental paradigm shift in barometric research, moving from imaging measurements before/after the pressurisation cycles to measurements performed during compression and decompression.

The described system could be useful for studies of physiological processes in live animals. However, some challenges remain. In particular, to avoided artifacts from movement, it is crucial that the animal stays perfectly still throughout the entire duration of a scan. However, because animals can rarely be trained to lie still for the duration of even shorter scans, anesthesia is often needed. Because CT, PET or MRI scans are not painful/harmful on their own, it is advantageous to use only very light anesthesia; especially during acquisition of physiological data that might be modified by anesthesia. It is beyond the scope of this study to discuss potential anesthesia methods, but we have promising preliminary experience from rodent experiments using intraperitoneal bolus injections of barbiturates (pentobarbiturate; 50 $mg \cdot kg^{-1}$) prior to pressure exposures. Furthermore, by fitting cannulas through pressure-tight cable penetrations it is possible to infuse fluids, providing a convenient route for administration of drugs and withdrawal of blood.

Conclusion

In conclusion, this study demonstrates a pressure chamber system compatible with CT, PET and MRI to collect morphological and physiological data non-invasively. Implementation of these advanced in-vivo imaging techniques in barometric research will provide new insights into fundamental mechanisms associated with acute direct and indirect effects of pressure exposure, including characterisation of haemodynamic effects and metabolic consequences in various tissues. We envisage that the described system could be of value for studies of the biological effects of gases in various fields, including: general anaesthesia;[22] inert gas narcosis;[23–25] oxygen toxicity;[26] gas poisoning (e.g., cyanide and carbon monoxide[27]); multiple indications treated with hyperbaric oxygen therapy[28–30] and differential pressure-related effects (e.g., the initial stages of the high pressure nervous syndrome[31] and DCS[32]).

References

1 Djasim UM, Spiegelberg L, Wolvius EB, van der Wal, KGH. A hyperbaric oxygen chamber for animal experimental purposes. *Int J Oral Max Surg*. 2012;41:271-4.

2 Rech FV, Fagundes DJ, Hermanson R, Rivoire HC, Fagundes ALN. A proposal of multiplace hyperbaric chamber for animal experimentation and veterinary use. *Acta Cir Bras*. 2008;23:384-90.

3 Reimers Systems, INC. {Internet]. *MRI Compatible Chambers* [updated 2014, cited 2015 June 7]. Available from: http://www.reimersystems.com/#!mri-compatible-chambers/cpdn

4 Aksoy FG. MR imaging of subclinical cerebral decompression sickness. A case report. *Acta Radiol*. 2003;44:108-10.
5 Havnes MB, Widerøe M, Thuen M, Torp SH, Brubakk AO, Møllerløkken A. Simulated dive in rats lead to acute changes in cerebral blood flow on MRI, but no cerebral injuries to grey or white matter. *Eur J Appl Physiol*. 2013;113:1405-14.
6 Gao GK, Wu D, Yang Y, Yu T, Xue J, Wang X, Jiang YP. Cerebral magnetic resonance imaging of compressed air divers in diving accidents. *Undersea Hyperb Med*. 2009;36:33-41.
7 Moen G, Specht K, Taxt T, Sundal E, Grønning M, Thorsen E, et al. Cerebral diffusion and perfusion deficits in North Sea divers. *Acta Radiol*. 2010;51:1050-8.
8 Grønning M, Aarli JA. Neurological effects of deep diving. *J Neurol Sci*. 2011;304:17-21.
9 Jersey SL, Baril, RT, McCarty RD, Millhouse CM. Severe neurological decompression sickness in a U-2 pilot. *Aviat SpaceEnvir Med*. 2010;81:64-8.
10 Blogg SL, Loveman GA, Seddon FM, Woodger N, Koch A, Reuter M, et al. Magnetic resonance imaging and neuropathology findings in the goat nervous system following hyperbaric exposures. *Eur Neurol*. 2004;52:18-28.
11 Matsumoto KI, Bernardo M, Subramanian S, Choyke P, Mitchell JB, Krishna MC, Lizak MJ. MR assessment of changes of tumor in response to hyperbaric oxygen treatment. *Magn Reson Med*. 2006;56:240-6.
12 Muir ER, Cardenas D, Huang S, Roby J, Li G, Duong TQ. MRI under hyperbaric air and oxygen: effects on local magnetic field and relaxation times. *Magn Reson Med*. 2014;72:1176-81.
13 Moore, MJ, Hammar T, Arruda J, Cramer S, Dennison S, Montie E, Fahlman A. Hyperbaric computed tomographic measurement of lung compression in seals and dolphins. *J Exp Biol*. 2011;214:2390-7.
14 Liu X, Yu L, Primak AN, McCollough CH. Quantitative imaging of element composition and mass fraction using dual-energy CT: three-material decomposition. *Med Phys*. 2009;36:1602-9.
15 Bockisch A, Beyer T, Antoch G, Freudenberg LS, Kühl H, Debatin JF, Müller SP. Positron emission tomography/computed tomography–imaging protocols, artifacts and pitfalls. *Mol Imaging Biol*. 2004;6:188-99.
16 Muir ER, Zhang Y, San Emeterio Nateras O, Peng Q, Duong TQ. Human vitreous: MR imaging of oxygen partial pressure. *Radiology*. 2013;266:905-11.
17 Zaharchuk G, Busse RF, Rosenthal G, Manley GT, Glenn OA, Dillon WP. Noninvasive oxygen partial pressure measurement of human body fluids in vivo using magnetic resonance imaging. *Acad Radiology*. 2006;13:1016-24.
18 Hopkins AL, Yeung HN, Bratton CB. Multiple field strength in vivo T1 and T2 for cerebrospinal fluid protons. *Magn Reson Med*. 1986;3:303-11.
19 Bloch F, Hansen WW, Packard M. The nuclear induction experiment. *Physiol Rev*. 1946;70:474-85.
20 Mirhej ME. Proton spin relaxation by paramagnetic molecular oxygen. *Can J Chemistry*. 1965;43:1130-8.
21 Battino R, Clever HL. The solubility of gases in liquids. *Chem Rev*. 1966;66:395-463.
22 Ruzicka J, Beneš J, Bolek L, Markvartova V. Biological effects of noble gases. *Physiol Res*. 2007;56:39-44.
23 23. Behnke AR, Thomas RM, Motley EP. The psychologic effect from breathing air at 4 atmospheres pressure. *Am J Physiol*. 1935;112:554-8.
24 Bennet PB, Rostain JC. Inert gas narcosis. In: Brubakk AO, Neuman TS, editors. *Bennett and Elliott's physiology and medicine of diving*. Edinburgh: Saunders;2003. p. 300-22.
25 Rostain, JC, Balon N. Recent neurochemical basis of inert gas narcosis and pressure effects. *Undersea Hyperb Med*. 2006;33:197-204.
26 Stadie WC, Riggs BC, Haugaard N. Oxygen poisoning. *Am J Med Sci*. 1944;207:84-113.
27 Lawson-Smith P, Jansen EC, Hilsted L, Hyldegaard O. Effect of hyperbaric oxygen therapy on whole blood cyanide concentrations in carbon monoxide intoxicated patients from fire accidents. *Scand J Trauma Resusc Emerg Med*. 2010;18:2-6.
28 Grim PS, Gottlieb LJ, Boddie A, Batson E. Hyperbaric oxygen therapy. *JAMA*. 1990;263:2216-20.
29 Thom SR. Hyperbaric oxygen: Its mechanisms and efficacy. *Plast Reconstr Surg*. 2011;127:131S-41S.
30 Thom SR. Oxidative stress is fundamental to hyperbaric oxygen therapy. *J Appl Physiol*. 2009;106:988-95.
31 Bennett PB, Rostain JC. The high pressure nervous syndrome. In: Brubakk, AO, Neuman TS. *Bennett and Elliott's physiology and medicine of diving*. Edinburgh: Saunders;2003. p. 323-57.
32 Vann RD, Butler FK, Mitchell SJ, Moon RE. Decompression illness. *Lancet*. 2011;377:153-64.

Acknowledgments

We thank Rene Wind and Hans Jørgen Hvid (Sjellerupskov, Denmark) for their enthusiastic technical assistance; Hans Erik Hansen and Thomas Hansen are acknowledged for help with custom-made adaptors and equipment crucial for the automatic pressure control system and Jonas L Andersen's assistance during the production of Figure 1. The Helga og Peter Kornings Fond supported the developmental phase of the system.

Conflicts of interest: nil

Submitted: 15 January 2015; revised 18 June 2015
Accepted: 17 August 2015

Kasper Hansen[1,2,3], Esben SS Hansen[1,3,7], Lars P Tolbod[4], Martin C Kristensen[5], Steffen Ringgaard[1,3], Alf O Brubakk[6], Michael Pedersen[1,2]

[1] Institute for Clinical Medicine, Aarhus University, Aarhus N, Denmark
[2] Comparative Medicine Lab, Aarhus University, Aarhus N, Denmark
[3] MR Research Centre, Aarhus University, Aarhus N, Denmark
[4] Department of Nuclear Medicine & PET-Center, Aarhus University Hospital, Aarhus N, Denmark
[5] Department of Procurement & Clinical Engineering, Central Denmark Region, Aarhus N, Denmark
[6] Department of Circulation and Medical Imaging, Norwegian University of Science and Technology, Trondheim, Norway
[7] Danish Diabetes Academy, Odense, Denmark

Address for correspondence:
Kasper Hansen
Comparative Medicine Lab and Institute for Clinical Medicine
Palle Juul-Jensens Boulevard 99
DK-8200 Aarhus N
Denmark
E-mail: *<kasperhansen@clin.au.dk>*